



# Tephra horizons identified in the western North Atlantic and Nordic Seas during the Last Glacial Period: Extending the marine tephra framework

Sunniva Rutledal<sup>a, b, \*</sup>, Sarah M.P. Berben<sup>a, b</sup>, Trond M. Dokken<sup>b, c</sup>,  
Willem G.M. van der Bilt<sup>a, b</sup>, Jan Magne Cederstrøm<sup>a, b</sup>, Eystein Jansen<sup>a, b, c</sup>

<sup>a</sup> Department of Earth Science, University of Bergen, Allégaten 41, 5007, Bergen, Norway

<sup>b</sup> Bjerknes Centre for Climate Research, Jahnebakken 5, 5007, Bergen, Norway

<sup>c</sup> Norwegian Research Centre (NORCE), Jahnebakken 5, 5007, Bergen, Norway

## ARTICLE INFO

### Article history:

Received 6 November 2019

Received in revised form

25 February 2020

Accepted 25 February 2020

Available online 17 March 2020

### Keywords:

Tephrochronology

Cryptotephra

Tephrostratigraphy

Tephra isochrons

FMAZ II

NAAZ II

Geochemistry

Paleoceanography

Marine sediment cores

Quaternary

North Atlantic Ocean

## ABSTRACT

Geochemically distinct volcanic ash (tephra) deposits are increasingly acknowledged as a key geochronological tool to synchronize independent paleoclimate archives. Recent advances in the detection of invisible (crypto) tephra have led to the ongoing establishment, development and integration of regional tephra lattices. These frameworks offer an overview of the spatial extent of geochemically characterized tephra from dated eruptions – a valuable tool for precise correlation of paleorecords within these areas. Here, we harness cryptotephra analysis to investigate the occurrence of two well-known tephra markers from the Last Glacial Period (i.e. FMAZ II-1 (26.7 ka b2k) and NAAZ II (II-RHY-1) (55.3 ka b2k)), in marine sediment cores from the Nordic, Irminger and Labrador Seas. In addition, we assess the imprint of bioturbation on two of these tephra deposits using Computed Tomography (CT) imagery. We have successfully identified FMAZ II-1 in the Nordic and Irminger Seas. The tephra deposit is a visible deposit in the Nordic Seas, whereas it appears as a single high concentration peak within the fine-grained shard size fraction (i.e. 25–80 μm) in the Irminger Sea. Both horizons are primary airfall deposits, and this study is the first to identify a FMAZ II-1 deposit of isochronous nature in the Irminger Sea region. In addition, we have identified a new tephra horizon in the Irminger Sea, which is stratigraphically associated with FMAZ II-1, and geochemically similar to the known 2-JPC-192-1 population. We discuss its potential to serve as a new reference tie-point for correlations in the region. Lastly, we have successfully identified NAAZ II (II-RHY-1) of isochronous nature in both the Irminger and Labrador Sea. The layers are interpreted to be deposited by either direct airfall or by sea-ice drifting past the sites. Compared to the existing frameworks, which previously mainly focused on sites east of Iceland, our findings expand the knowledge and utility of the FMAZ II-1 and NAAZ II (II-RHY-1) horizons.

© 2020 The Authors. Published by Elsevier Ltd. This is an open access article under the CC BY license (<http://creativecommons.org/licenses/by/4.0/>).

## 1. Introduction

Tephrochronology, the use of synchronously deposited and geochemically fingerprinted ash horizons as time markers across geological archives, has become an increasingly recognized tool for correlating Late Quaternary climate records. Fundamentally, the detection of well-dated and geochemically distinct tephra horizons within disparate and/or distant records allows for an assessment of

the synchronicity of change during abrupt climate transitions in the past (Austin et al., 2012). Recent advances in cryptotephra (invisible to the naked eye) analysis (Davies, 2015), have resulted in the discovery of new chronological tie-points at more distal localities, further promoting the development of more detailed tephra frameworks (Bourne et al., 2015; Abbott et al., 2018a).

Tephra frameworks are a compilation of both visible and cryptotephra occurrences in distal and proximal settings. In addition, they provide an overview of the dispersal area of certain volcanic eruptions and of the past eruptive frequency of volcanoes in the region. Several tephra frameworks from the North Atlantic region already exist, such as the overview of tephra horizons identified in

\* Corresponding author. Department of Earth Science, University of Bergen, Allégaten 41, 5007, Bergen, Norway

E-mail address: [Sunniva.Rutledal@uib.no](mailto:Sunniva.Rutledal@uib.no) (S. Rutledal).



sites further to the west is required. Additionally, the latter would provide a more comprehensive picture of the ash dispersal across the broader northern North Atlantic Ocean during the Last Glacial Period.

The objective of this study is to further develop the existing North Atlantic tephra framework between 60 and 25 ka b2k previously presented by Abbott et al. (2018a). This objective is aimed for by examining the occurrence of FMAZ II-1 and NAAZ II (II-RHY-1) in marine sediment cores from the eastern (Nordic Seas) and western (Irminger and Labrador Sea) North Atlantic Ocean. In addition, we will assess the isochronous nature of these tephra layers and, as such, investigate whether they can act as independent time-markers (isochrons) for future correlation to other records.

## 2. Materials and methods

### 2.1. Marine sediment cores

In this study, we carried out tephra investigations on three marine sediment cores from the North Atlantic Ocean (i.e. MD99-2284, GS16-204-18CC and GS16-204-22CC) (Fig. 1). Core MD99-2284, was retrieved with the R/V *Marion Dufresne* in the eastern part of the Nordic Seas, north of the Faroe-Shetland Channel, at a water depth of 1500 m (62° 22,48 N; 00° 58,81 W) (Dokken et al., 2013; Sadatzki et al., 2019). Marine sediment cores GS16-204-18CC and GS16-204-22CC were collected during the ice2ice-2016 cruise aboard R/V *G.O. Sars* within the western part of the North Atlantic Ocean, south of Greenland. GS16-204-18CC was retrieved within the Irminger Sea at 2220 m water depth along the southeast Greenland margin (60° 01,84 N; 40° 33,45 W), whereas GS16-204-22CC was collected in the Labrador Sea at 3160 m water depth on the southern flank of the Eirik Drift (58° 02,83 N; 47° 02,36 W).

### 2.2. Selection of marine core depth-intervals

Previously developed chronologies for all investigated cores allowed us to target the time intervals, and thus core depths, where we expect FMAZ II-1 and NAAZ II (II-RHY-1) to be deposited.

#### 2.2.1. MD99-2284

The position of a black tephra layer between 1404 and 1409 cm in MD99-2284, stratigraphically possibly correlating to FMAZ II-1, was first visually identified and reported by Dokken et al. (2013). Nonetheless, its geochemical composition has, so far, never been analyzed. The first visual appearance of ash at the base of the layer was used as the tephra marker horizon (i.e. 1408–1409 cm).

#### 2.2.2. GS16-204-18CC

Samples with the potential of containing FMAZ II-1 and NAAZ II (II-RHY-1) material in GS16-204-18CC were carefully selected using the magnetic susceptibility record (Dokken and Cruise-Members, 2016) which records cycles of Greenland Interstadials (GI) and Greenland Stadials (GS) (Voelker and Hafliadason, 2015). To further support the sampling interval selection, we analyzed concentrations of ice rafted debris (IRD) and planktic foraminifera  $\delta^{18}\text{O}$  values (Lisa Griem pers. commun 20.08.2018). Subsequently, light isotope events that mark the stratigraphic position of Heinrich events were used, supporting a preliminary age model. Based on this evidence, we selected the intervals 210–250 cm and 505–525 cm, stratigraphically located between GI-3 and GI-2, after Heinrich event 3 and GI-15, respectively, for tephra analysis.

#### 2.2.3. GS16-204-22CC

The existing age model for GS16-204-22CC, presented by Griem

et al. (2019) was constructed by tuning GS16-204-22CC to marine sediment core PS2644, previously collected within the Denmark Strait (Voelker et al., 1998) using planktic  $\delta^{18}\text{O}$  and  $\delta^{13}\text{C}$  isotopes. Based on that age model, the depth-intervals 191–210 cm (23.4–27.5 ka b2k (FMAZ II-1)) and 463–479 cm (54.3–55.8 ka b2k (NAAZ II (II-RHY-1))) were selected for tephra analysis.

### 2.3. Tephra analysis

Sediment samples from depth-intervals that fall within the age range of the targeted tephra deposits were sampled as 0.5 cm (GS16-204-18/22CC) and 1 cm (MD99-2284) slices at 1 cm intervals. An exception was made for core GS16-204-18CC (250–210 cm) that initially was sampled at 2 cm intervals, and in the case of increased tephra shard concentrations at 1 cm. The samples were first freeze-dried and homogenized. Subsequently, ca 0.5 g dry weight of material from each sample was prepared for tephra analysis following the methodology for marine tephra deposits (Abbott et al., 2011, 2018b). To remove carbonate material, dilute (10%) hydrochloric acid (HCl) was added to each sample and left overnight (~12 h). Samples were subsequently sieved into three size fractions (i.e. >125  $\mu\text{m}$ , 80–125  $\mu\text{m}$  and 25–80  $\mu\text{m}$ ). The fine-grained size fraction (25–80  $\mu\text{m}$ ) was then separated into different density fractions (i.e. >2.5 g/cm<sup>3</sup>, 2.3–2.5 g/cm<sup>3</sup> and <2.3 g/cm<sup>3</sup>) using heavy liquid flotation with sodium polytungstate (SPT). This technique is applied to separate rhyolitic (2.3–2.5 g/cm<sup>3</sup>) from basaltic (>2.5 g/cm<sup>3</sup>) glass shards (Turney, 1998; Blockley et al., 2005). Using the methodology from Griggs et al. (2014), the >2.5 g/cm<sup>3</sup> fraction was magnetically separated using a Frantz Isodynamic Magnetic Separator in an effort to separate the paramagnetic basaltic shards from the non-magnetic minerogenic material. Finally, each sample was mounted on glass slides using Canada Balsam. If tephra shard concentrations exceeded 10.000 shards/g, the preparation steps described previously were repeated and lycopodium spore tablet(s) were added to the 25–80  $\mu\text{m}$  fraction after the final density separation step. The required number of tablets varied (1–2 tablets) but the aim was to ensure that >300 spores were represented on each microscope slide. Then, to allow total dissolution of the spore tablet(s) the sample was soaked in ca. 5 ml HCl, where after it was washed and rinsed three times to ensure that the remaining HCl was completely removed. To ensure a representative range of the sample, three drops of the sample, with the material in suspension, were mounted on a microscope slide. Eventually, all tephra shards and lycopodium spores on the microscope slide were counted after Gehrels et al. (2006). The relative amount of tephra shards was calculated using equation (2.1), where  $l$  is the number of lycopodium spores in each tablet ( $n = 18\,584 \pm 354$ , batch no. 177745).

Concentration =  $l$

$$\times \left( \frac{\text{glass shard count}}{\text{Lycopodium spore count} \times \text{sample dry weight}} \right) \quad (2.1)$$

For each analyzed depth interval, peaks in the tephra shard concentration profiles were selected for major element analysis. After repeating the previously described preparation steps, the samples were embedded in epoxy resin on frosted microprobe slides. To expose the surface of the glass tephra shards, the mounted material was ground using p1000 silicon carbide paper and polished using  $\frac{1}{4}$   $\mu\text{m}$  diamond polycrystalline suspension. Individual tephra shards were analyzed using Electron-probe microanalysis (EPMA). These measurements were performed at the Tephrochronological Analytical Unit at the University of Edinburgh using a Cameca SX100 electron microprobe with five vertical wavelength dispersive spectrometers, providing oxide values (wt.

%) for 10 major elements (see supplementary information). Approximately 20–40 individual shards per sample were analyzed following the protocols outlined by Hayward (2012). Based on the sample's shard size, a 3  $\mu\text{m}$  or 5  $\mu\text{m}$  beam diameter was used (see supplementary information). To monitor analytical precision, glass standards (Lipari Obsidian (rhyolitic) and BCR2g (basaltic)) were measured regularly. For geochemical data comparison, the data was normalized to 100% total oxides. All raw data values are given in the supplementary information. Totals below 94% and 97% for rhyolitic and basaltic material, respectively, were rejected.

The major element data (oxides expressed as wt. %) was statistically compared to previously published geochemical populations using statistical distance (SD) and similarity coefficient (SC) tests following the methods outlined in Perkins et al. (1995) and Borchardt et al. (1972), respectively. In addition, graphical examination using bi-plots was carried out. When calculating the SC's, we only included elements with concentrations >1 wt %. Traditionally, values between 0.95 and 1 have been interpreted as identical dataset; whereas values between 0.90 and 0.95 as not identical dataset, but most likely originate from the same volcanic source (Davis, 1985; Beget et al., 1992). However, it should be noted that for Icelandic Volcanic systems, Abbott et al. (2018a) only accept SC's higher than 0.97 as identical geochemical compositions. The SD function considers the differences between two datasets and can only be used to assess if two populations are different and thus, not that they are the same. The calculated values are compared to critical values (=18.48 (rhyolitic) and = 23.21 (basaltic)) at a 99% confidence level. The difference in the critical values between rhyolitic and basaltic material is a result of comparing major element oxides with an average value higher than 0.1 wt % (10 elements for basaltic and 7 elements for rhyolitic material). If the statistical distance value is higher than the critical value, the datasets are considered to be different. If the value is lower than the critical value the datasets are not considered to be different, but not necessarily identical (Pearce et al., 2008). In addition to statistical tests, the stratigraphic position of the tephra horizons in the different marine sequences were also considered when correlating deposits.

#### 2.4. Ice rafted debris

In ice-proximal areas like the studied region, icebergs provide a possible transport pathway for tephra shards that eventually hamper the isochronous nature of a tephra horizon. Therefore, to evaluate the influence of tephra transported to the region by icebergs, we generated IRD records for the same depth intervals as investigated for the tephra analysis. This combination of IRD and tephra shard concentration profiles will offer insight to whether or not a tephra peak results from ice-rafting transport to the study sites (represented by increased IRD) (Griggs et al., 2014; Abbott et al., 2018b). For GS16-204-18CC we constructed a new IRD record (lithic grains between 150 and 500  $\mu\text{m}$ ) using the standard method of split counting (Heinrich, 1988; Bond and Lotti, 1995). For GS16-204-22CC, we used the IRD record presented in Griem et al. (2019).

#### 2.5. Computed Tomography (CT) scanning

We visualize the imprint of bioturbation and IRD on parts of the cores GS16-204-18CC (510–529.5 cm) and GS16-204-22CC (452.5–488.5 cm), using Computed Tomography (CT) after e.g. Griggs et al. (2015). To do so, we employed a ProCon X-Ray CT-ALPHA scanner, operated at 100 kV and 850  $\mu\text{A}$  and using a 267 ms exposure time. To capture sub-millimeter scale features, we minimized the distance between the detector and source by

scanning 2 cm wide u-channels. Reconstructed 16 bit scans were processed with the Thermo Scientific™ Avizo™ 9.1.1 software suite. First, we selected specific CT grayscale ranges with the *threshold* tool to highlight the density of hollow burrows (air) and ice rafted debris (clastic). For this purpose, we relied on the grayscale intensity histograms of our scans after Griggs et al. (2015): the lightest (low grayscale) peak corresponds to air, while the densest (high grayscale) peak reflects clastic material. To warrant correct interpretation, the outcome of this iterative process was compared to visual evidence of hollows and rock particles in the scanned core segments. Next, we created 3-D visualizations of thresholded (highlighted) CT grayscale ranges (features) using the *volume rendering* tool. Finally, we used the sieving tool to remove isolated voxels with a diameter smaller than 400  $\mu\text{m}$  to reduce cluttering (noise), before visualizing highlighted features using a combination of 2-D ortho slices and 3-D visualizations after Van der Bilt et al. (2018).

#### 2.6. Evaluating the isochronous nature of tephra deposits

Tephra shards can be transported to the marine realm by a range of different pathways and during the Last Glacial Period, in our study areas, this was predominantly via direct aerial ash fall-out, by icebergs or sea-ice (Griggs et al., 2014). However, tephra layers are also susceptible to secondary depositional mechanisms such as remobilization of material by bioturbation and/or strong bottom currents. To be able to use tephra layers as time-markers, they need to be deposited and incorporated in the sediment sequence near-instantaneously following an eruption. In this study, we evaluate tephra layers with respect to their potential primary and secondary depositional mechanisms following the newly introduced classification scheme on deposit types outlined by Abbott et al. (2018b). They classified tephra deposits into five different types common in North Atlantic marine sequences. The five deposit types are summarized in Table 1. A type 1 deposit is defined as a well-constrained, low concentration shard peak with homogeneous composition, representing one single depositional event most likely deposited by primary airfall. A type 2 deposits reveals a distinct high concentration peak in shard concentration with an upward or downward spanning of shards and is either geochemically homogeneous (2A) or heterogeneous (2B). The deposit represents one single depositional event, but can be subjected to secondary reworking. The transport mechanism of this deposit type must be evaluated based on the geochemical composition as primary airfall, sea-ice rafting and iceberg rafting is possible. A type 3 deposit typically shows a flat bottom profile with an upward tailing of shards, a very high shard concentration and a geochemically homogeneous composition. Secondary reworking and/or bioturbation cause the gradual upward tailing and the most likely transport mechanism is either primary airfall or sea-ice rafting. A type 4 deposit has high shard concentrations and reveals multiple peaks over a large spread (10s of cm). Such a deposit type likely represents either several closely spaced eruptions or deposition by icebergs. A type 5 deposit has a wide spread of consistent shard concentrations, which typically represents a background signal. These shards are most likely reworked and remobilized within the ocean system, which could mask low concentration peaks representing single volcanic events.

### 3. Results

The tephra deposits identified in this study are summarized in Table 2.

**Table 1**Overview of the tephra deposit type classification scheme used in this study after [Abbott et al. \(2018b\)](#).

Deposit type	Characteristics and transport/deposition	Useful isochron?
Type 1	<ul style="list-style-type: none"> <li>Well constrained, low concentration shard peak</li> <li>Homogeneous geochemical composition</li> <li>Most likely deposited by primary airfall</li> </ul>	Yes
Type 2	<ul style="list-style-type: none"> <li>Clear high concentration shard peak</li> <li>Upward and downward tailing of shards</li> <li>Geochemically homogeneous (2A) or heterogeneous (2B)</li> <li>Could be transported and deposited by sea-ice rafting, iceberg rafting or primary airfall</li> </ul>	Yes, if homogeneous geochemistry
Type 3	<ul style="list-style-type: none"> <li>High concentration of shards. Flat bottom with upward tailing.</li> <li>Geochemically homogeneous</li> <li>Most likely transported by primary airfall or sea-ice rafting.</li> <li>No IRD peaks</li> </ul>	Yes
Type 4	<ul style="list-style-type: none"> <li>Distribution of multiple high concentration peaks</li> <li>Large deposit spread</li> <li>Either several closely spaced eruptions or iceberg rafted tephra.</li> </ul>	Yes, if peaks can be tied to the Greenland tephra framework. The tephra peaks also have potential as regional marine tie-lines.
Type 5	<ul style="list-style-type: none"> <li>Background signal of consistent low shard concentration.</li> <li>Geochemically heterogeneous</li> <li>Reworking and remobilization within the ocean system.</li> </ul>	No, but potential isochrons could be masked by the background signal.

**Table 2**Summary of tephra deposits investigated in this study with respect to their isochronous integrity, deposit type, climatic event, correlative isochrons and volcanic source. GS = Greenland stadial, GI = Greenland interstadial, H=Heinrich event. References are as follows: (1) this study; (2) [Wastegård et al. \(2006\)](#); (3) [Davies et al. \(2008\)](#); (4) [Griggs et al. \(2014\)](#); (5) [Brendryen et al. \(2011\)](#); (6) [Abbott et al. \(2018a\)](#); (7) [Abbott et al. \(2016\)](#); (8) [Austin et al. \(2004\)](#); (9) [Grönvold et al. \(1995\)](#).

Tephra deposit	Climatic event	Deposit Type	Useful isochron?	Correlative isochron	Volcanic source	Reference (s)
MD99-2284 (1408–1409 cm)	GS-3	Visible/Type 3	Yes	FMAZ II-1	Hekla/Vatnafjöll	1,2,3,4
GS16-204-18CC (228.5–229 cm, 25–80 µm)	GS-3	Type 2A	Yes	FMAZ II-1	Hekla/Vatnafjöll	1,2,3,4
GS16-204-18CC (225.5–226 cm, >125 µm)	GS-3	Type 2A	Yes	2-JPC-192-1 (?)	Bárdarbunga-Veidivötn or Reykjanes	1,2
GS16-204-22CC (191–210 cm)	Post H3	Type 5	No			1
GS16-204-18CC (512.5–513 cm)	GI-15	Type 2A	Yes	NAAZ II (II-RHY-1)	Torfajökull	1,2,5,6,7,8,9
GS16-204-22CC (474–474.5 cm)	GI-15	Type 3	Yes	NAAZ II (II-RHY-1)	Torfajökull	1,2,5,6,7,8,9

### 3.1. FMAZ II-1

#### 3.1.1. MD99-2284

The tephra deposit in core MD99-2284 has a sharp visual boundary between the tephra layer and the underlying sediments as well as a visible upward tailing of decreasing tephra shards ([Fig. 2B](#)). Tephra shards from the base (1408–1409 cm) of the visible layer have been geochemically analyzed for major elements.

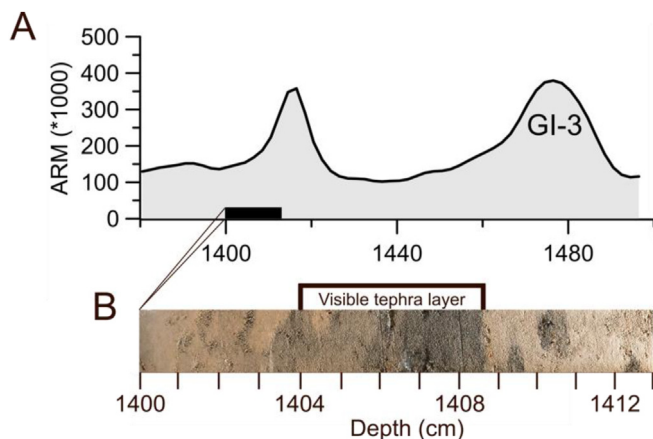


**Fig. 2.** A: Anhyseretic remanent magnetization (ARM) (log scale/unit  $10^{-6}$  A/m) in MD99-2284 (1380–1500m) from [Dokken et al., \(2013\)](#) plotted against depth (cm). GI-3 = Greenland Interstadial 3. B: Image of the visual tephra layer in MD99-2284 (1404–1409 cm).

The tephra shard geochemistry reveals a basaltic homogeneous composition in the three different grain size fractions analyzed (i.e. >125 µm, 80–125 µm, 25–80 µm) ([Fig. 3](#)). Characteristic features of selected oxides (expressed as wt. %) include contents of ca. 49–51 wt. % SiO<sub>2</sub>, ca. 3.4–3.8 wt. % TiO<sub>2</sub>, ca. 4.2–5.6 wt. % MgO, ca. 8.5–9.8 wt. % CaO, ca. 0.3–0.7 wt. % K<sub>2</sub>O and FeO/MgO ratios between 2.6 and 3.6. This geochemical signature exhibits strong affinities with the Hekla-Vatnafjöll volcanic system in the Eastern Volcanic Zone (EVZ), SW Iceland ([Jakobsson, 1979](#); [Larsen, 1981](#)). Using the similarity coefficient (SC) and statistical distance (SD) function we evaluate (1) how well the MD99-2284 (1408–1409 cm) tephra shard geochemistry correlates to the FMAZ II-1 suite reported in previous studies and (2) if the MD99-2284 (1408–1409 cm) basaltic horizon can be considered identical to previous reports of the FMAZ II-1 tephra shard geochemistry (i.e. SC between 0.95 and 1 and SD < 23.21; see section 2.3). The statistical results show SC's ranging from 0.94 to 0.98 and SD's ranging from 6.78 to 14.84 ([Table 3](#)). Hence, the tephra shard geochemistry from MD99-2284 (1408–1409 cm) correlates with the FMAZ II-1 suite reported from both a Greenland ice-core ([Davies et al., 2008](#)) and several North Atlantic marine records ([Wastegård et al., 2006](#); [Griggs et al., 2014](#)). This correlation can also visually be observed in the geochemical biplots ([Fig. 3B](#)) where selected major element oxides from MD99-2284 (1408–1409 cm) plot within the FMAZ II-1 geochemical field.

The stratigraphic and geochemical features of the MD99-2284 (1408–1409 cm) deposit are consistent with a deposit type 3 ([Table 1](#)), which is most likely transported via primary airfall or sea-ice rafting. The visibility of the layer and thus the immense

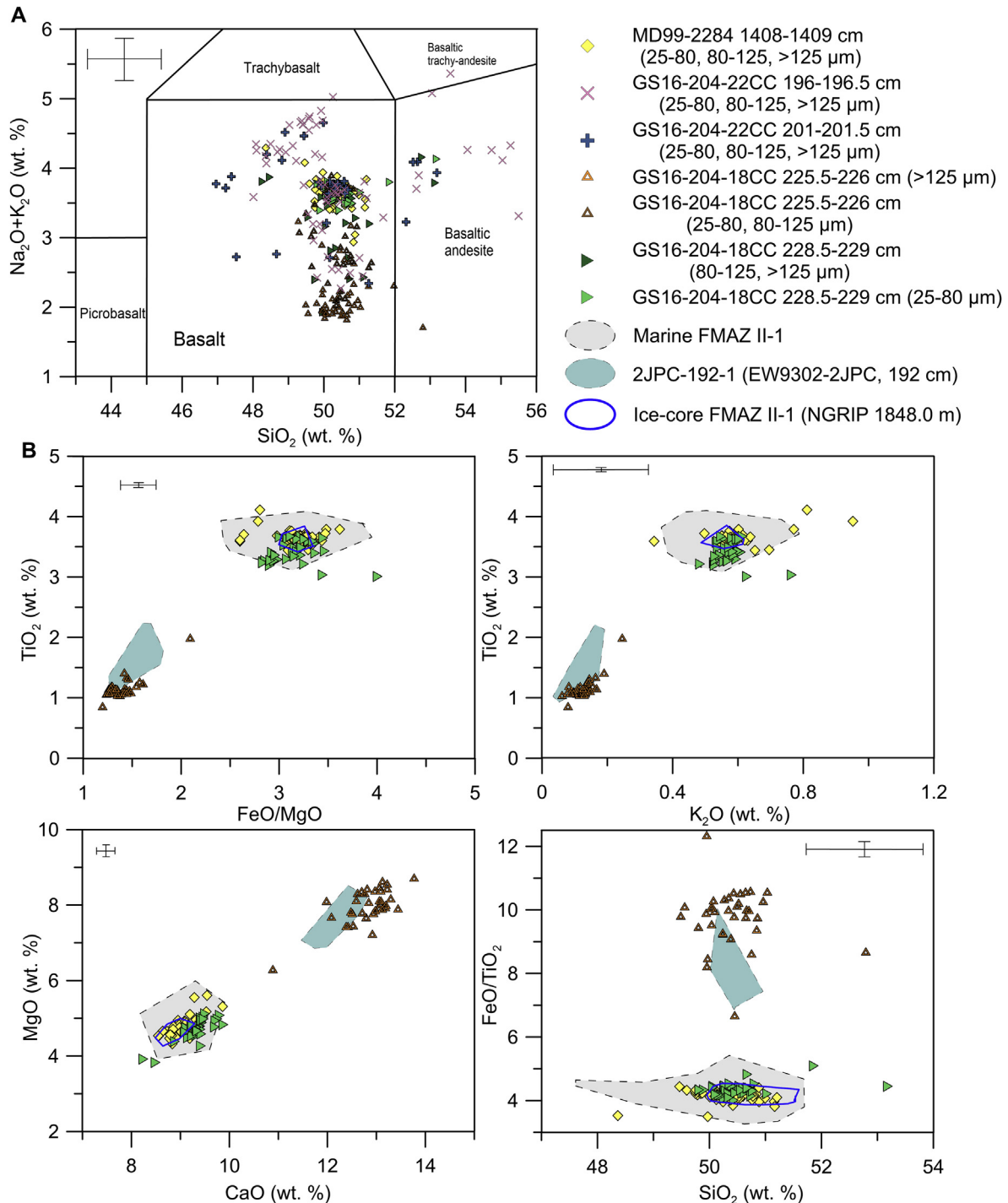


**Fig. 3.** Tephra shard geochemistry from cores MD99-2284 (1408–1409 cm), GS16-204-18CC (225.5–226 cm and 228.5–229 cm) and GS16-204-22CC (196–196.5 cm and 201–201.5 cm). A: Total alkali silica (TAS) plot of the chemical composition of tephra shards from MD99-2284 (1408–1409 cm), GS16-204-18CC (225.5–226 cm and 228.5–229 cm) and GS16-204-22CC (196–196.5 cm and 201–201.5 cm). Chemical classification and nomenclature from [Le Maitre and Bateman \(1989\)](#) B: Visual biplot comparison of tephra shard analyses (major element oxides) from GS16-204-18CC (228.5–229 cm) and MD99-2284 (1408–1409 cm) to the FMAZ II-1 geochemical data from the North Atlantic marine tephra framework (grey shaded area) ([Wastegård et al., 2006](#); [Griggs et al., 2014](#)) and from the Greenland ice core NGRIP (blue circle), ([Davies et al., 2008](#)). In addition, the tephra shard geochemistry from GS16-204-18CC (225.5–226 cm, >125  $\mu\text{m}$ ) is compared to the 2-JPC-192-1 geochemical data (blue area) from [Wastegård et al., \(2006\)](#). Error bars represents 2 standard deviations of replicate analyses of BC2rg reference glass. (For interpretation of the references to colour in this figure legend, the reader is referred to the Web version of this article.)

concentration of shards argue for a primary airfall deposition although sea-ice rafting cannot be fully excluded. Nonetheless, as the potential temporal delay by sea-ice rafting (months to years) is shorter than the chronological resolution within marine sequences

([Brendryen et al., 2010](#)), neither of these potential transport processes are considered to cause a significant temporal delay. Thus, this deposit contains all the required characteristics to be defined as an isochron.

**Table 3**

Statistical comparison of the geochemical compositions from the basaltic layers of MD99-2284 (1408–1409 cm) and GS16-204-18CC (228.5–229 cm, 25–80  $\mu\text{m}$ ) with the FMAZ II-1 population in North Atlantic marine records and the Greenland ice-core record. In addition, statistical comparison of the geochemical compositions of the rhyolitic layers in GS16-204-18CC (512.5–513 cm) and GS16-204-22CC (474–475 cm) with the NAAZ II (II-RHY-1) population in North Atlantic marine records and the Greenland ice-core record.

	FMAZ II-1				NAAZ II (II-RHY-1)			
	MD99-2284 (1408–1409 cm)		GS16-204-18CC (228.5–229 cm, 25–80 $\mu\text{m}$ )		GS16-204-18CC (512.5–513 cm)		GS16-204-22CC (474–475 cm)	
	SC	SD	SC	SD	SC	SD	SC	SD
NGRIP (1848 m) Davies et al. (2008)	0.96	8.57	0.96	8.81	–	–	–	–
JM11-19 PC (Griggs et al., 2014)	0.98	6.96	0.97	22.31	0.97	4.12	0.98	9.72
ENAM 93-20 (Wastegård et al., 2006)	0.97	9.99	0.97	5.27	0.94	<b>21.47</b>	0.93	<b>23.72</b>
ENAM 93-21 (Wastegård et al., 2006)	0.97	14.84	0.97	8.96	–	–	–	–
ENAM 33 (Wastegård et al., 2006)	0.94	6.78	0.94	7.33	0.94	<b>19.87</b>	0.93	<b>20.85</b>
LINK 17 (Wastegård et al., 2006)	0.98	8.30	0.96	12.20	–	–	–	–
LINK 04 (Wastegård et al., 2006)	0.98	11.65	0.98	5.92	–	–	–	–
EW 9302-2JPC (Wastegård et al., 2006)	0.96	12.28	0.96	7.74	0.92	15.78	0.91	17.11
MD95-2006 (Austin et al., 2004)	–	–	–	–	0.95	14.59	0.94	16.01
SO82-05/B-3 (Brendryen et al., 2011)	–	–	–	–	0.94	3.77	0.92	7.12
SO82-05/A-1 (Brendryen et al., 2011)	–	–	–	–	0.97	6.09	0.96	11.29
SO82-05/B-2 (Brendryen et al., 2011)	–	–	–	–	0.98	1.98	0.96	7.92
SO82-05/A-4 (Brendryen et al., 2011)	–	–	–	–	0.98	2.03	0.96	6.37
MD99-2289 (Brendryen et al., 2011)	–	–	–	–	0.98	5.19	0.96	4.20
MD04-2820CQ (Abbott et al., 2016)	–	–	–	–	0.98	1.26	0.98	2.77
MD04-2822 (Abbott et al., 2018a)	–	–	–	–	0.97	0.48	0.95	2.81
MD95-2024 (Abbott et al., 2018a)	–	–	–	–	0.98	0.99	0.96	3.55
MD99-2251 (Abbott et al., 2018a)	–	–	–	–	0.98	1.19	0.98	3.41
M23485-1 (Abbott et al., 2018a)	–	–	–	–	0.98	0.34	0.99	2.74
MD01-2461 (Abbott et al., 2018a)	–	–	–	–	0.98	0.46	0.98	3.22
MD95-2010 (Abbott et al., 2018a)	–	–	–	–	0.98	2.55	0.99	1.40
GIK23415-9 (Abbott et al., 2018a)	–	–	–	–	0.99	0.84	0.98	2.64
GRIP (2430.95 m) Grönvold et al. (1995)	–	–	–	–	0.94	1.84	0.96	1.78

### 3.1.2. GS16-204-18CC

The tephrostratigraphy for GS16-204-18CC (210–250 cm) is presented in Fig. 4. Between 225.5 cm and 229 cm a basaltic tephra horizon is observed in all size fractions. However, within the fine-grained size fraction (i.e. 25–80  $\mu\text{m}$ ), the basaltic tephra concentration peak occurs between 228.5 and 229 cm. In contrast, within the coarser-grained size fractions (i.e. >125  $\mu\text{m}$  and 80–125  $\mu\text{m}$ ), both concentration peaks appear 3 cm upwards, between 225.5 and 226 cm. Tephra shards from all size fractions from the depth intervals that capture a concentration peak were geochemically analyzed for major elements.

**3.1.2.1. GS16-204-18CC: 228.5–229 cm.** The geochemical composition of the tephra shards from the fine-grained size fraction (i.e. 25–80  $\mu\text{m}$ ) of GS16-204-18CC (228.5–229 cm) shows, with the exception of two outliers, a homogeneous basaltic geochemistry (Fig. 3B). Distinct geochemical characteristics of the analyzed tephra layer are FeO/MgO ratios of ca. 2.8–3.4, ca. 49–51 wt. % SiO<sub>2</sub>, ca. 3.1–3.7 wt. % TiO<sub>2</sub>, ca. 4.2–5.1 wt. % MgO, ca. 8.8–9.8 wt. % CaO, and ca. 0.5–0.6 wt. % K<sub>2</sub>O. These characteristics are comparable to the signature of the Hekla-Vatnafjöll volcanic system (Jakobsson, 1979; Larsen, 1981). The calculated SC's and SD's from the comparison between the tephra shard geochemistry of GS16-204-18CC (228.5–229 cm, 25–80  $\mu\text{m}$ ) and of FMAZ II-1 from both a Greenland ice-core (Davies et al., 2008) and several North Atlantic marine records (Wastegård et al., 2006; Griggs et al., 2014) are 0.94–0.97 and 5.2–22, respectively (Table 3). These values are indicative of a correlation between the deposits. This correlation is also observed in the geochemical biplots (Fig. 3B), which reveals a strong visual correlation between selected major element oxides and the FMAZ II-1 geochemical field. The tephra shard

geochemistry from the coarser-grained size fractions (i.e. >125 and 80–125  $\mu\text{m}$ ) of GS16-204-18CC (228.5–229 cm) shows a heterogeneous basaltic geochemistry with SiO<sub>2</sub> values between 47.6 and 52.33 wt % (Fig. 3A). Although, we note that half (14/28) of these shards have a similar geochemistry as the fine-fraction (i.e. FMAZ II-1) (see supplementary).

One single high concentration peak with a homogeneous geochemistry and no up- or downward tailing of shards characterizes the fine-grained (i.e. 25–80  $\mu\text{m}$ ) tephra deposit from 228.5 to 229 cm. In addition, the concentration peak does not co-occur with any peaks in the IRD record (Fig. 4). This evidence is most consistent with a type 2A deposit (Table 1). Such a deposit is most likely transported and deposited by primary airfall or sea-ice rafting, which cause no significant temporal delay after the eruption. Therefore, this deposit is defined as an isochron.

**3.1.2.2. GS16-204-18CC: 225.5–226 cm.** Concerning the tephra deposit found 3 cm upwards between 225.5 and 226 cm, the tephra shard geochemistry from the two smallest size fractions (i.e. 80–125  $\mu\text{m}$  and 25–80  $\mu\text{m}$ ) is basaltic and heterogeneous. For instance, SiO<sub>2</sub> values range from 48 to 51.3 wt % (Fig. 3A). Of these shards, six (of 39) have a geochemistry similar to FMAZ II-1, which is recorded 3 cm earlier. These FMAZ II-1 shards are likely deposited as a result of secondary transport mechanisms such as reworking and/or iceberg rafting. On the other hand, the geochemistry from the coarser-grained shards (i.e. GS16-204-18CC, 225.5–226 cm; >125  $\mu\text{m}$ ) shows, with the exception of two outliers, a fairly homogeneous basaltic composition. Representative features are normalized values of ca. 49.5–51 wt. % SiO<sub>2</sub>, ca. 1–1.4 wt. % TiO<sub>2</sub>, ca. 7.4–8.6 wt. % MgO, ca. 12–13.7 wt. % CaO, ca. 0.06–0.16 wt. % K<sub>2</sub>O and FeO/MgO ratios between 1.2 and 1.6 (Fig. 3B). This geochemical

## GS16-204-18CC (Irminger Sea)

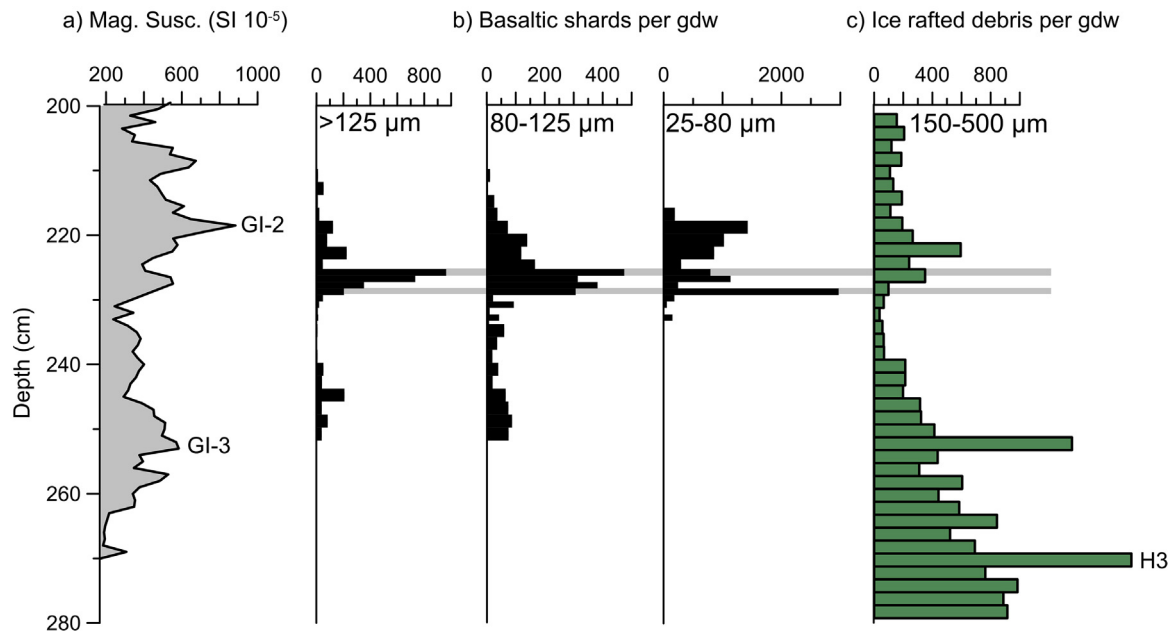


**Fig. 4.** Summary of marine sediment core GS16-204-18CC from the Irminger Sea. a) Magnetic susceptibility ( $10^{-5}$  Si units) of GS16-204-18CC (200–270 cm) (Dokken and Cruise-Members, 2016). GI = Greenland Interstadial. b) Tephrostratigraphy of GS16-204-18CC (210–250 cm, 2 cm resolution and 224.5–234.5 cm, 1 cm resolution) plotted versus depth (cm). The concentration of basaltic shards per gdw (gram dry weight) is quantified in three different size fractions (i.e.  $>125 \mu\text{m}$ ,  $80\text{--}125 \mu\text{m}$  and  $25\text{--}80 \mu\text{m}$  ( $>2.5 \text{ g/cm}^3$ )). c) Ice rafted debris per gdw from the  $150\text{--}500 \mu\text{m}$  size fraction of GS16-204-18CC (200–280 cm, every 2 cm). H3 refers to Heinrich event 3. Grey horizontal line marks the position of the two tephra horizons at 225.5–226 cm and at 228.5–229 cm that were geochemically analyzed.

composition is distinctly different from the FMAZ II-1 population identified 3 cm lower in the core, respectively at 228.5–229 cm. This geochemical signature suggests an origin from either the Bardarbunga-Veidivötn volcanic system in the Eastern Volcanic Zone (EVZ) (Jakobsson, 1979; Óladóttir et al., 2011) or the Reykjanes volcanic system in the Western Volcanic Zone (WVZ) (Jakobsson et al., 1978) (see supplementary figures). The only report of a tephra deposit that is stratigraphically related to the FMAZ II-1 isochron, but has a distinctly different geochemistry is the 2-JPC-192-1 deposit from the Labrador Sea (core EW9302-2JPC) (Wastegård et al., 2006). Statistical comparison between this deposit and the GS16-204-18CC (225.5–226 cm,  $>125 \mu\text{m}$ ) geochemical population reveals a SC of 0.90 and a SD of 7.02. The low SC value of 0.90 indicates that the geochemical signatures are not similar. The small number of measurements ( $n = 7$ ) from the 2-JPC-192-1 layer (Wastegård et al., 2006) offers a limited dataset for statistical comparison which might explain the low SC. Nonetheless, the 2-JPC-192-1 and GS16-204-18CC (225.5–226 cm,  $>125 \mu\text{m}$ ) populations could also represent different, but closely spaced eruptions from the same volcanic center. The tephra shard concentration profile of this deposit shows a high concentration peak with tailing of shards a few centimeters downwards (Fig. 4). In addition, the deposit co-occurs with increased peaks in IRD concentration, which is indicative of iceberg transport to the site. However, geochemical data from the  $>125 \mu\text{m}$  fraction reveals a fairly homogeneous population. This particular deposit was most likely not deposited by icebergs as iceberg-rafted deposits often exhibit a heterogeneous geochemistry. These results argue for a type 2A deposit (Table 1), which most likely is transported to the site by primary airfall or sea-ice rafting. These are transport and depositional mechanisms that do not affect the isochronous integrity of the deposit and therefore, the deposit is defined as an isochron.

### 3.1.3. GS16-204-22CC

The tephra shard concentration profile from GS16-204-22CC (191–210 cm) reveals in all size fractions a continuous background signal of basaltic tephra shards ( $<500$  shards/g) (Fig. 5b). A minor tephra shard concentration peak was observed between 196 and 196.5 cm in all size fractions and therefore, shard material from this depth was prepared for geochemical analysis. In addition, based on increasing concentrations in the  $>125 \mu\text{m}$  size fraction, tephra shards from the 201–201.5 cm interval was geochemically analyzed.

**3.1.3.1. GS16-204-22CC: 201–201.5 cm.** The tephra shard geochemistry from the fine-grained size fraction (i.e.  $25\text{--}80 \mu\text{m}$ ) from GS16-204-22CC (201–201.5 cm) shows a heterogeneous geochemistry (Fig. 3A). For instance, normalized  $\text{SiO}_2$  values vary between 47.5 wt. % and 53.1 wt. %. However, 11 out of 17 measurements of the geochemical analyses form a tight homogeneous sub-population with values of ca. 49.9–50.6 wt. %  $\text{SiO}_2$ , ca. 3.5–3.7 wt. %  $\text{TiO}_2$ , ca. 4.37–4.84 wt. %  $\text{MgO}$ , ca. 8.74–9.20 wt. %  $\text{CaO}$ , ca. 0.52–0.64 wt. %  $\text{K}_2\text{O}$  and  $\text{FeO/MgO}$  ratios between 3.12 and 3.46. This suggests similarities to the Hekla-Vatnafjöll volcanic system (Larsen, 1981; Jakobsson, 1979). A statistical comparison between this homogeneous sub-population and the FMAZ II-1 geochemistry from a Greenland ice-core (Davies et al., 2008) and several North Atlantic marine records (Wastegård et al., 2006; Griggs et al., 2014) reveals SC's between 0.93 and 0.98 and SD's between 0.25 and 1.15, which are indicative of a correlation (Table 3). Geochemical analyses of shards from the two coarser-grained size fractions (i.e.  $>125 \mu\text{m}$  and  $80\text{--}125 \mu\text{m}$ ) of GS16-204-22CC (201–201.5 cm) reveal a basaltic heterogeneous geochemistry (Fig. 3A). Five (of 15) of these shards correlate to the FMAZ II-1 geochemical suite and are likely deposited as a product of secondary transport mechanisms.

## GS16-204-22CC (Labrador Sea)

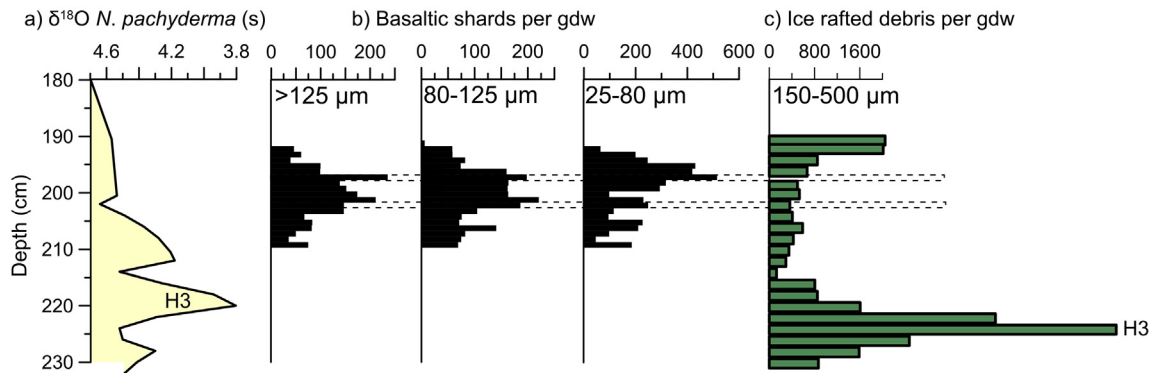


**Fig. 5.** Summary of marine sediment core GS16-204-22CC from the Labrador Sea. a)  $\delta^{18}\text{O}$  record of the planktic foraminifera *Neogloboquadrina pachyderma sinistral* (*N. pachyderma* (s)) for GS16-204-22CC from (Griem et al., 2019). H3 = Heinrich event 3. b) Tephrostratigraphy of GS16-204-22CC (191–210 cm, 1 cm resolution) plotted versus depth (cm). The concentration of basaltic shards per gdw (gram dry weight) is quantified in three different size fractions (i.e. >125  $\mu\text{m}$ , 80–125  $\mu\text{m}$  and 25–80  $\mu\text{m}$  (>2.5  $\text{g/cm}^3$ )). c) Ice rafted debris per gdw from the 150–500  $\mu\text{m}$  size fraction of GS16-204-18CC (200–280 cm, every 2 cm). Dotted horizontal lines mark the position of the two depth intervals, 196–196.5 cm and 201–201.5 cm, that were geochemically analyzed.

**3.1.3.2. GS16-204-22CC: 196–196.5 cm.** The geochemical composition of GS16-204-22CC (196–196.5 cm) is basaltic and heterogeneous across all size fractions (i.e. 25–80  $\mu\text{m}$ , 80–125  $\mu\text{m}$  and >125  $\mu\text{m}$ ). For example,  $\text{SiO}_2$  values range between 48 and 55 wt. % and thus, this heterogeneous geochemistry represents tephra material derived from a mix of volcanic sources (Fig. 3A). One dominant source is the FMAZ II-1 eruption as 19 (of 67) shards correlate to this isochron.

The GS16-204-22CC (191–210 cm) tephrostratigraphy is characterized by a consistent background concentration of tephra shards with no clear concentration peak. In addition, the tephra shard concentration is low (<500 shards/g) and generally the geochemistry of the measured intervals is heterogeneous. The upper part of the deposit (191–196 cm) coincides with increased levels of IRD concentrations. This evidence argues for a type 5 deposit (Table 1), which has most likely been influenced by post-depositional reworking and remobilization, potentially masking smaller tephra shard concentration peaks. Possibly, the analyzed tephra shards from the fine-grained size fraction between 201 and 201.5 cm that correlate to the FMAZ II-1 horizon are such a masked deposit. However, due to the remobilization of this material, the deposit cannot be convincingly correlated to the FMAZ II-1 isochron.

## 3.2. NAAZ II

### 3.2.1. GS16-204-18CC

The tephra shard concentration profile of GS16-204-18CC (505–525 cm) reveals a rhyolitic deposit in the 25–80  $\mu\text{m}$  and >125  $\mu\text{m}$  size fractions between 511 and 518 cm (Fig. 6). We find a distinct high concentration peak between 512.5 cm and 513 cm (Fig. 6) and analyzed tephra shards from this high concentration peak as well as from the base of the deposit between 517.5 cm and 518 cm. Due to the immense shard concentrations the size fraction 80–125  $\mu\text{m}$  was not counted.

The shard geochemistry from GS16-204-18CC (512.5–513 cm) and GS16-204-18CC (517.5–518 cm) both reveal a similar rhyolitic homogeneous composition with characterizing major element values of ca. 74.8–76.3 wt. %  $\text{SiO}_2$ , ca. 2.4–2.9 wt. % FeO, ca. 0.3–0.45 wt. % CaO and ca. 4.5–5.7 wt. %  $\text{Na}_2\text{O}$  (Fig. 7). These characteristics are similar to the geochemical signature of the Thórsmörk Ignimbrite, from which the NAAZ II (II-RHY-1) suite likely derives (Sigurdsson, 1982; Lacasse et al., 1996) and now is

attributed to the Torfajökull volcano in the Eastern Volcanic Zone (EVZ) (Moles et al., 2019). The geochemistry of the rhyolitic tephra of GS16-204-18CC (512.5–513 cm) was statistically compared to the geochemical data from the NAAZ II (II-RHY-1) population in a Greenland ice-core (Grönvold et al., 1995) and several North Atlantic marine records (Austin et al., 2004; Wastegård et al., 2006; Brendryen et al., 2011; Abbott et al., 2018a). The results yield SC's of 0.92–0.99 and SD's ranging between 0.3 and 21.4 supporting a correlation between the GS16-204-18CC (512.5–513 cm) tephra layer and the NAAZ II (II-RHY-1) isochron (Table 3). There are some offsets between the geochemical analyses of this study and older analyses like those presented in Wastegård et al. (2006). The latter contributes to similarity coefficients lower than 0.95 and statistical distance values over 18.48. In particular, the analyses from GS16-204-18CC (512.5–513 cm) display lower  $\text{Al}_2\text{O}_3$  and  $\text{SiO}_2$  values as well as higher  $\text{Na}_2\text{O}$  concentrations. Some of these differences are most likely caused by the sodium (Na) loss effect during older analyses (Hunt and Hill, 2001; Hayward, 2012). These results corresponds to previous reports by Abbott et al. (2016). Therefore, comparisons with more recent analyses should be prioritized.

On either side of the main concentration peak we identify a high number of rhyolitic tephra shards (Fig. 6). Evidence from the high-resolution CT-scan between 510 and 529.5 cm, which identified 0.5–1 cm elongated burrows positioned just below the main concentration peak between 512.5 and 513 cm, indicate that bioturbation has been an active process in this section of the core and the downward tailing of shards could be a product of this activity (Fig. 8A). The geochemistry of the deposit is homogeneous, and there is no IRD peak coinciding with the concentration peak. These results are indicative of a type 2A deposit (Table 1) hinting at two possible transport mechanisms: (1) the tephra was transported to the site directly by airfall or (2) the tephra was transported by primary airfall onto sea-ice that most likely drifted to the site along the East Greenland Current (EGC) (Fig. 1). Although the proximity to the Icelandic source and the presence of a relatively high concentration of coarse shards (>125  $\mu\text{m}$ ) argue stronger for sea-ice rafting, deciphering between the two transport mechanisms is at this point not possible. However, in either scenario, there is no significant temporal delay of deposition after the eruption that would affect the integrity of the isochron.

### 3.2.2. GS16-204-22CC

The GS16-204-22CC (455–479 cm, >125  $\mu\text{m}$  and 25–80  $\mu\text{m}$ )

## GS16-204-18CC (Irminger Sea)

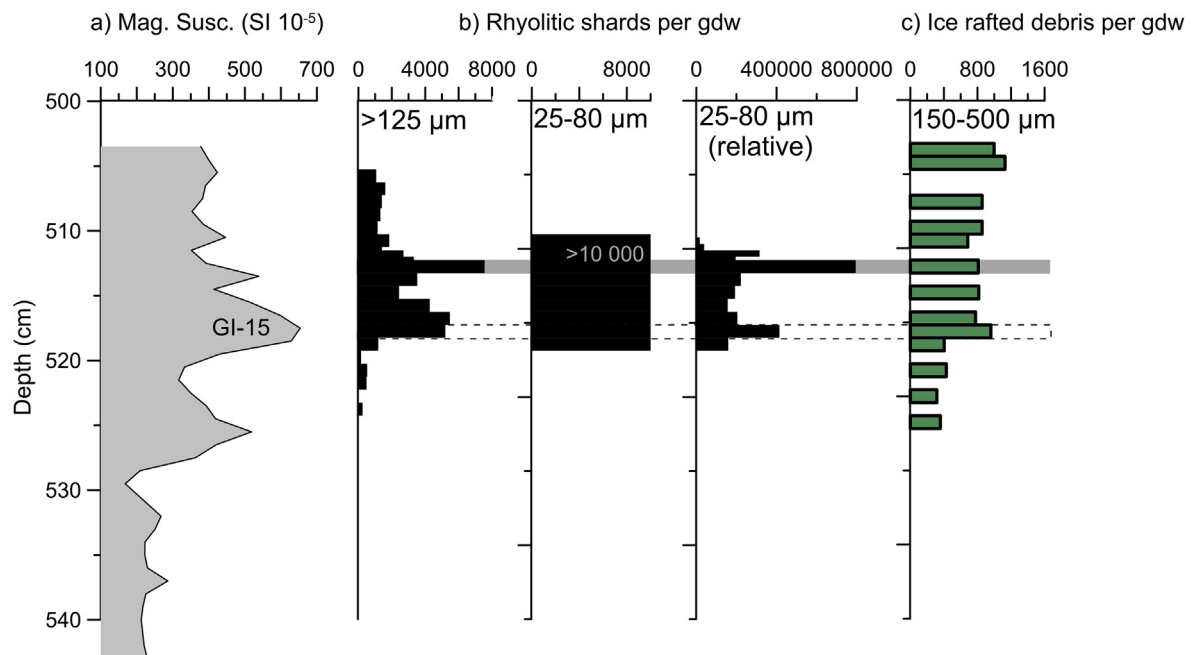


**Fig. 6.** Summary of marine sediment core GS16-204-18CC from the Irminger Sea. a) Magnetic susceptibility ( $10^{-5}$  Si units) from GS16-204-18CC (500–540 cm) (Dokken and Cruise-Members, 2016). GI = Greenland Interstadial. b) Tephrostratigraphy from GS16-204-18CC (505–525 cm) plotted versus depth (cm). The concentration of rhyolitic shards per gdw (gram dry weight) is quantified in two different size fractions (i.e.  $>125 \mu\text{m}$  and  $25\text{--}80 \mu\text{m}$  ( $2.3\text{--}2.5 \text{g/cm}^3$ )). Note that the middle panel refers to the level of shard counts  $>10,000/\text{g}$ , which were treated with lycopodium to achieve the panel on the right. c) Ice rafted debris per gdw from the  $150\text{--}500 \mu\text{m}$  size fraction from GS16-204-18CC (502–522 cm). Grey horizontal line marks the position of the tephra isochron. The dotted horizontal line marks the position of peaks geochemically analyzed in addition to the main peak.

tephrostratigraphy shows a relatively flat-bottomed profile with an upward tailing of tephra shards starting from a high concentration peak between 474 cm and 474.5 cm. The deposit is positioned between 469 and 474.5 cm (Fig. 9b) and the main rhyolitic shard maximum is observed between 474 cm and 474.5 cm in both size fractions (i.e.  $>125 \mu\text{m}$  and  $25\text{--}80 \mu\text{m}$ ). Due to the extensive shard concentrations, the size fraction  $80\text{--}125 \mu\text{m}$  was not counted. Tephra shards from the main concentration peak (474–474.5 cm) and from neighbouring samples (473–473.5 cm and 470–470.5 cm) were geochemically analyzed for major elements in order to assess the relationship to the main concentration peak.

Geochemical analysis reveals a similar homogenous rhyolitic geochemistry for all analyzed depth intervals. Characteristic geochemical features from the main concentration peak between 474 and 474.5 cm are values of ca. 75–76 wt. %  $\text{SiO}_2$ , ca. 2.4–2.9 wt. % FeO, ca. 0.3–0.5 wt. % CaO and ca. 4.9–5.8 wt. %  $\text{Na}_2\text{O}$  (Fig. 9). This geochemical signature can be linked to the Thórsmörk Ignimbrite from the Torfajökull volcano in the Eastern Volcanic Zone (EVZ) (Sigurdsson, 1982; Lacasse et al., 1996; Moles et al., 2019). To determine whether the GS16-204-22CC (474–474.5 cm) rhyolitic layer can indeed be correlated to the NAAZ II (II-RHY-1) population, we compared its geochemistry to the geochemical signature of NAAZ II (II-RHY-1) from a Greenland ice-core (Grönvold et al., 1995) and several North Atlantic marine records (Austin et al., 2004; Wastegård et al., 2006; Brendryen et al., 2011; Abbott et al., 2018a). Similar as for NAAZ II (II-RHY-1) in GS16-204-18CC, high SD numbers for two of the comparisons can be attributed to sodium (Na) loss in the older analyses. We calculate SC's between 0.91 and 0.99 and SD's between 1.4 and 23.72, which indicate a correlation between the GS16-204-22CC (474–474.5 cm) rhyolitic tephra layer and the NAAZ II (II-RHY-1) isochron (Table 3).

The high resolution CT-scan of GS16-204-22CC (452.5–488.5 cm) reveals 1–2 cm elongated burrows upwards

from 474 to 474.5 cm (Fig. 8B). The presence of burrows at this level in the core verifies bioturbation as an active process that could cause the upward tailing of tephra shards identified in the tephra shard concentration profile. In addition, there are no IRD peaks coinciding with the tephra deposit. These characteristics indicate a type 3 deposit (Table 1), which was most likely deposited by primary airfall or sea-ice rafting. Subsequently, the tephra deposit is useful as an isochron.

#### 4. Discussion

##### 4.1. Expanding the North Atlantic tephra framework covering the Last Glacial Period

###### 4.1.1. FMAZ II-1

Both the visible tephra layer recorded in MD99-2284 (1408–1409 cm) from the Nordic Seas and the fine-grained fraction ( $25\text{--}80 \mu\text{m}$ ) in GS16-204-18CC (228.5–229 cm) are of isochronous nature and can be correlated to the established geochemistry of the FMAZ II-1 horizon in the literature. Similar to our results in MD99-2284 (1408–1409 cm), FMAZ II-1 appears as a thick and visible layer in many records from the Nordic Seas and Faroe region (Kuijpers et al., 1998; Rasmussen et al., 2003; Wastegård et al., 2006; Griggs et al., 2014). In fact, previous marine investigations of airfall deposited FMAZ II-1 have mainly focused on the latter region, and this study is the first to observe primary airfall deposited FMAZ II-1 in the Irminger Sea (GS16-204-18CC). With the new data presented, we expand the known dispersal range of the FMAZ II-1 tephra towards the west (Fig. 1).

Close in depth to the FMAZ II-1 isochron in GS16-204-18CC we find a coarse-grained homogenous basaltic tephra layer with geochemical characteristics similar to the 2-JPC-1-192 layer, previously reported mixed with the FMAZ II-1 horizon in the Labrador

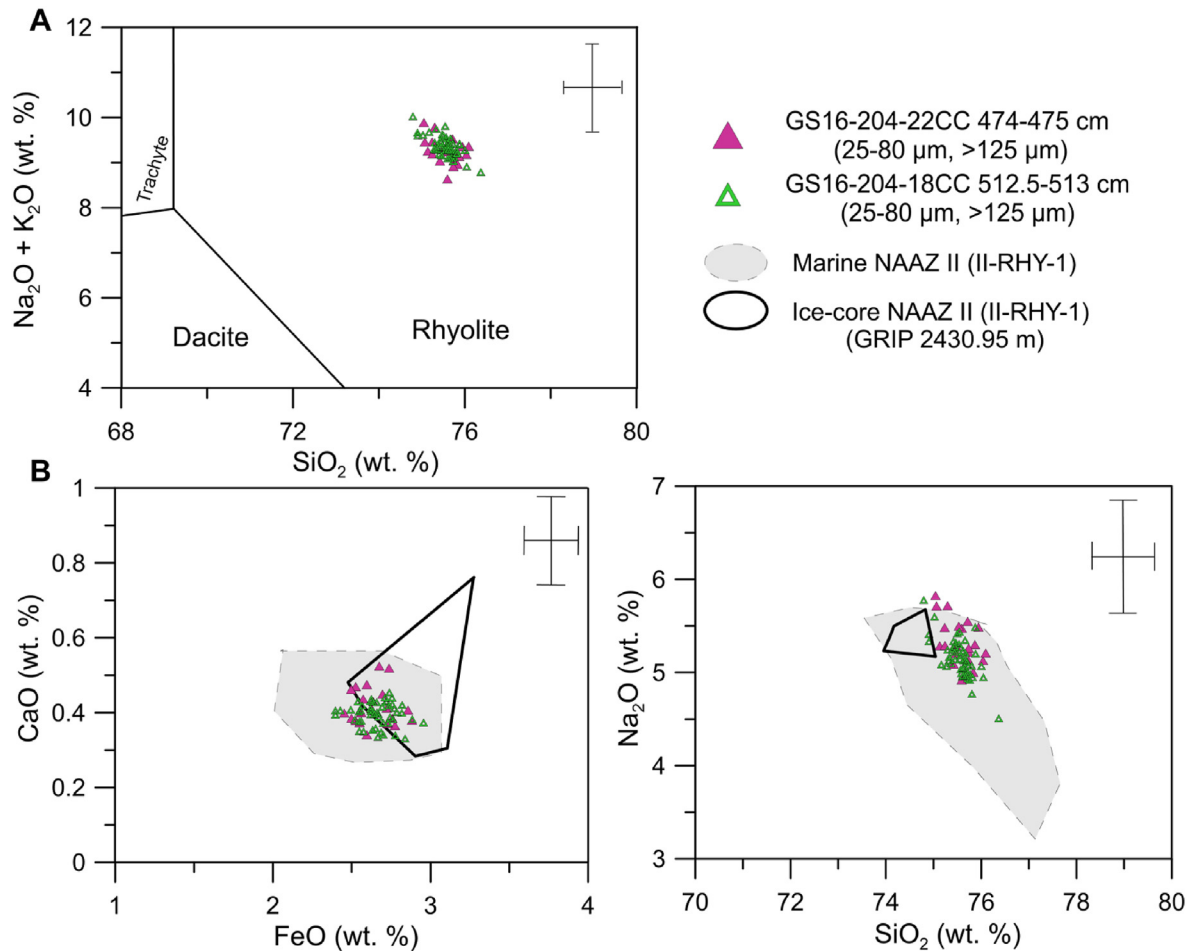


**Fig. 7.** Tephra shard geochemistry from cores GS16-204-18CC (474–4 cm) and GS16-204-22CC (512.5–513 cm). A: Total alkali silica (TAS) plot of the chemical composition of tephra shards from cores GS16-204-18CC (474–4 cm) and GS16-204-22CC (512.5–513 cm). Chemical classification and nomenclature from Le Maitre and Bateman (1989). B: Visual biplot comparison of tephra shard analyses (major element oxides) GS16-204-18CC (474–4 cm) and GS16-204-22CC (512.5–513 cm) to the NAAZ II (II-RHY-1) geochemical data from the North Atlantic marine tephra framework (grey shaded area) (Austin et al., 2004; Wastegård et al., 2006; Brendryen et al., 2011; Abbott et al., 2016, 2018a) and from the Greenland ice core GRIP (black line) (Grönvold et al., 1995). Error bars represent 2 standard deviations of replicate analyses of Lipari Obsidian reference glass.

Sea (Wastegård et al., 2006). However, a clear statistical correlation between the 2-JPC-1-192 layer and 225.5–226 cm (>125  $\mu\text{m}$ ) layer in GS16-204-18CC cannot be ascertained. Still, with additional geochemical data from these horizons, they may be linked in the future. The tephra from these two horizons appears only as coarser tephra grains (>125/150  $\mu\text{m}$ ) and is restricted to the areas south/southwest of Iceland (i.e. Irminger and Labrador Sea). Nonetheless, attempts have been made to discover the horizon in cores from the Faroe Island region and the Reykjanes ridge (Griggs et al., 2014). The occurrence of coarser grains and the, so far, exclusive recordings southwest of Iceland argue for more local eruption(s) and a regional transport mechanism that transported the tephra material from Iceland and solely to the southwesterly sites. We suggest that the tephra material was predominantly carried westwards by winds and deposited on sea-ice that drifted along the EGC (Fig. 1). In this manner, the material would only be distributed to the south-southwestern parts of the North Atlantic Ocean. Indeed, it has been suggested that in Greenland Stadials, during which FMAZ II-1 is deposited, a southward shift of the polar front allowed for the EGC to expand and divert southwards, carrying drifting sea-ice to more southerly sites than today (e.g. to core EW 9302-2JPC in the Labrador Sea) (Van Kreveld et al., 2000).

The investigations of FMAZ II-1 in core GS16-204-22CC (191–201 cm) from the Labrador Sea were inconclusive. Although

FMAZ II-1 material was present, the core depth-interval that recorded tephra showed evidence for remobilization and reworking of material, and no isochron could be determined. Either the lack of FMAZ II-1 material in GS16-204-22CC (191–201 cm) is a result of local remobilization of sediments or the core site is located outside the western limit of the primary FMAZ II-1 tephra distribution. However, in order to further investigate the FMAZ II-1 air-dispersal limits in a southwesterly direction, new efforts might be able to identify primary airfall deposited FMAZ II-1 layers southwest of our findings in the Irminger Sea in marine sediment cores that show no evidence of remobilization.

The largest and most updated MIS 3 and 2 North Atlantic tephra framework was presented by Abbott et al. (2018a) in which they investigated ten North Atlantic marine sediment cores. Within this framework, the FMAZ II-1 horizon is reported in one core from the southeastern Nordic Seas (JM11-19 PC) (Griggs et al., 2014). In the North Atlantic tephra framework by Wastegård et al. (2006), the FMAZ II-1 horizon (>150  $\mu\text{m}$ ) is reported in six cores. Five of the six cores within that framework are located in the region around the Faroe Islands whereas only one of them is located in the Labrador Sea. Hence, based on the existing tephra frameworks, there is no comprehensive understanding of the air dispersal pattern of FMAZ II-1 in a southwesterly direction from Iceland. In this study, we show that cryptotephra analysis allows the detection of the FMAZ

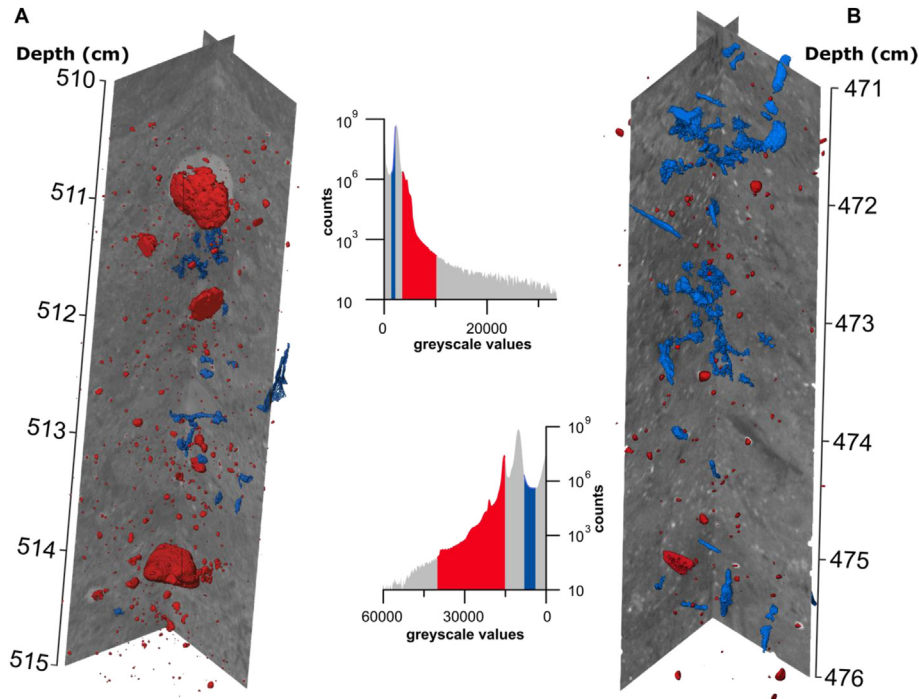


**Fig. 8.** Processed CT scan orthoslices of A: GS16-204-18CC (510–515 cm) and B: GS16-204-22CC (471–476 cm), with highlighted greyscale values in histograms showing IRD (red) and bioturbation (blue). Both IRD and bioturbation have been volume rendered to show the distribution and shape. (For interpretation of the references to colour in this figure legend, the reader is referred to the Web version of this article.)

### GS16-204-22CC (Labrador Sea)

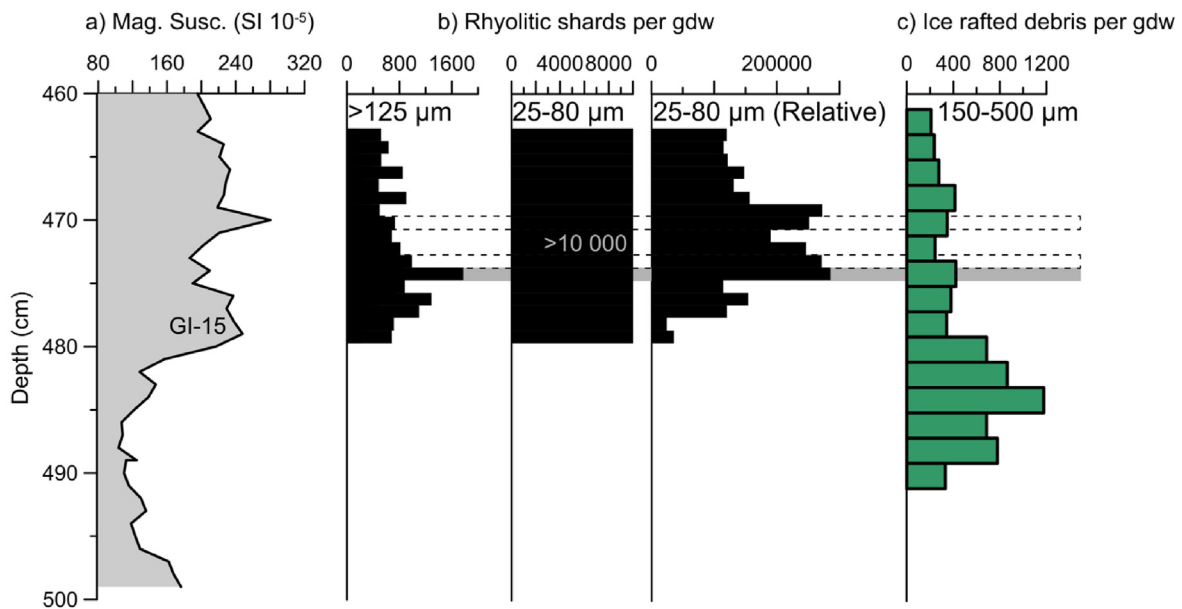


**Fig. 9.** Summary of marine sediment core GS16-204-22CC from the Labrador Sea. a) Magnetic susceptibility ( $10^{-5}$  Si units) from GS16-204-22CC (460–500 cm) (Dokken and Cruise-Members, 2016). GI = Greenland Interstadial. b) Tephrostratigraphy from GS16-204-22CC (463–479 cm) plotted versus depth (cm). The concentration of rhyolitic shards per gdw (gram dry weight) is quantified in two different size fractions (i.e.  $>125 \mu\text{m}$  and  $25\text{--}80 \mu\text{m}$  ( $2.3\text{--}2.5 \text{ g/cm}^3$ )). Note that the middle panel refers to the level of shard counts  $>10,000/\text{g}$ , which were treated with lycopodium to achieve the right panel. c) Ice rafted debris per gdw from the  $150\text{--}500 \mu\text{m}$  size fraction of GS16-204-22CC (460–490 cm). Grey horizontal line marks the position of the tephra isochron. The dotted horizontal lines mark the position of peaks geochemically analyzed in addition to the main peak.

II-1 horizon at sites on the western side of the North Atlantic Ocean. These results expand the tephra framework westwards and allow to link both sides of the North Atlantic Ocean (Fig. 10). Future investigations of FMAZ II-1 should preferentially focus on the

western side of the North Atlantic, as existing frameworks by Abbott et al. (2018a) and Wastegård et al. (2006) already cover most of the eastern side. In addition, we cautiously add a new tephra horizon to the framework that is associated with the FMAZ II-1

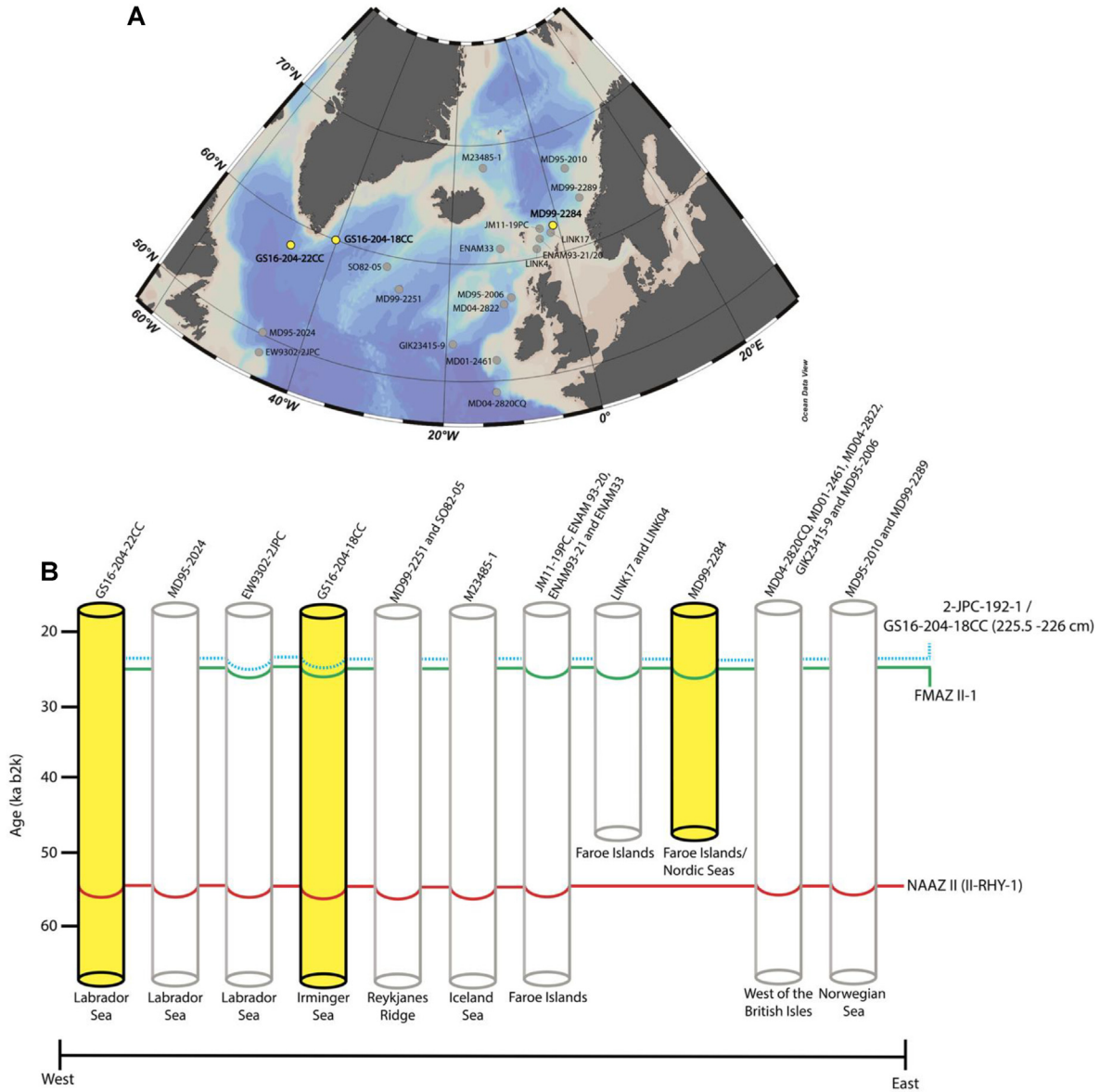


**Fig. 10.** A: Map of marine sediment cores in the new and improved North Atlantic tephra framework. References are as follows: GS16-204-22CC, GS16-204-18CC, MD99-2284 (this study), MD95-2024, MD99-2251, M23485-1, MD01-2461, MD04-2822, GIK23415-9, MD95-2010 (Abbott et al., 2018a). EW9302-2JPC, ENAM93-20, ENAM 93-21, ENAM33, LINK17, LINK04 (Wastegård et al., 2006). SO82-05 (Hafliðason et al., 2000; Brendryen et al., 2011). JM11-19 PC (Griggs et al., 2014; Abbott et al., 2018a). MD04-2820CQ (Abbott et al., 2016). MD95-2006 (Austin et al., 2004). MD99-2289 (Brendryen et al., 2011). Map was generated using the Ocean Data View software (<http://odv.awi.de/>). B: Schematic of the improved North Atlantic tephra framework after findings in this study, based on Fig. 2 in Abbott et al. (2018a). Newly identified tephra horizons by this study are marked in yellow core schematics, while the previously recorded tephra horizons from the existing North Atlantic tephra framework are marked in grey core schematics. For simplicity marine sediment cores from the existing North Atlantic tephra framework were grouped into geographical areas. Although the 2-JPC-192-1 and GS16-204-18CC (225.5–226 cm) horizons could not be convincingly correlated using statistical tests they most likely originate from the same volcanic source and are therefore here grouped together. Please note that the age scale is approximate. (For interpretation of the references to colour in this figure legend, the reader is referred to the Web version of this article.)

deposit, from the Irminger Sea (GS16-204-18CC, 225.5–226 cm, >125 μm). If this new horizon can be detected in more records, there is potential for a new reference horizon that can be used as a correlational tie-point in records from the south and southwest of Iceland. In addition, since this new horizon is stratigraphically linked to the more widespread FMAZ II-1 isochron, the horizon can be used to link records containing either one of the two horizons in future studies.

4.1.2. NAAZ II (II-RHY-1)

We correlate the rhyolitic deposits in GS16-204-18CC (512.5–513 cm) and GS16-204-22CC (474–474.5 cm) to the NAAZ

II (II-RHY-1) isochron. The NAAZ II (II-RHY-1) isochron has been identified in several sites across the North Atlantic Ocean and in the Greenland ice-core GRIP (Kvamme et al., 1989; Austin et al., 2004; Wastegård et al., 2006; Brendryen et al., 2011; Abbott et al., 2018a). At some of these sites, predominantly the more eastern ones basaltic/intermediate material is also present within the NAAZ II layer (Abbott et al., 2018a). The basaltic component of NAAZ II appears to be more pronounced at sites closer to the source and localities on the eastern side of the North Atlantic Ocean. Most likely the basaltic/intermediate material was transported to these sites by icebergs calving off the Icelandic ice sheet (Abbott et al., 2018a), which probably completely melted before reaching the more

south-southwestern core sites. This is consistent with the lack of a basaltic NAAZ II component in our sites in the Labrador and Irminger Sea.

Abbott et al. (2018a) report nine recordings of NAAZ II (II-RHY-1) within the North Atlantic marine tephra framework; five of these are from cores located west of the British Isles, two are from cores north and northeast of Iceland, and two are from sites south of Iceland (Gardar Drift and Labrador Sea). Within the North Atlantic tephra framework by Wastegård et al. (2006), the NAAZ II (II-RHY-1) isochron was identified in four cores; three of these cores are located in the Faroe Island region and one is from the Labrador Sea. In addition, Brendryen et al. (2011) contributes to the framework with NAAZ II (II-RHY-1) data from a site on the Reykjanes ridge, south of Iceland, as well as one site in the Nordic Seas (Fig. 10). A NAAZ II (II-RHY-1) horizon has also been inferred in the Irminger Sea (Elliot et al., 1998; Stoner et al., 1998); this reporting is, however, not substantiated with geochemical data. Our results therefore contribute to the North Atlantic tephra framework with new and updated geochemical data of the NAAZ II (II-RHY-1) horizon at localities that either fall outside the existing framework or are sparsely covered (Fig. 10). In addition, through the use of high-resolution CT-imagery, we determine that bioturbation most likely attributed to the tailing of shard concentrations in both deposits; this has not convincingly been shown in cores from the existing framework.

## 5. Conclusions

We have successfully identified the FMAZ II-1 isochron in MD99-2284 (1408–1409 cm) from the Nordic Seas and in GS16-204-18CC (228.5–229 cm, 25–80 µm) from the Irminger Sea. In contrast with sites in the Nordic Seas and Faroe Islands, where the FMAZ II-1 is recorded as a visible layer, the FMAZ II-1 is observed as a fine-fraction layer in the Irminger Sea (GS16-204-18CC, 228.5–229 cm, 25–80 µm). The discovery of FMAZ II-1 in the Irminger Sea is the first in the region and expands the previously known dispersal of the FMAZ II-1 tephra in a more northwesterly direction than showed by previous studies (Fig. 10A). This result broadens the North Atlantic tephra framework westwards and offers a new strategically located tie-point between the eastern and western side of the North Atlantic Ocean. Close in depth to our discovery of the FMAZ II-1 tephra in the Irminger Sea, a tephra deposit was recorded in the >125 µm size fraction (GS16-204-18CC, 225.5–226 cm). The geochemical composition of this coarser layer shows characteristics similar to 2-JPC-192-1 from the Labrador Sea. This horizon, found in stratigraphic proximity to FMAZ-II-1, has so far only been found southwest of Iceland. We suggest that tephra shards from these horizons were distributed from Iceland on sea-ice via the EGC, limiting the dispersal in a southwestward direction. Potentially, this new horizon can act as a reference horizon for correlation of records if more occurrences are fingerprinted in the region. We have also successfully identified the NAAZ II (II-RHY-1) in GS16-204-18CC (512.5–513 cm) from the Irminger Sea and in GS16-204-22CC (474–474.5 cm) from the Labrador Sea. These findings contribute to the North Atlantic tephra framework with new and updated geochemical data from the NAAZ II (II-RHY-1) isochron in the region. In addition, in order to better understand secondary reworking processes, we show how high-resolution CT-imagery can be used to visualize small-scale bioturbation above and below tephra isochrons.

In total, we report three different tephra horizons in three North Atlantic marine sediment cores that all possess an isochronous nature. All of these layers have potential to be used as time-markers or correlational tie-points in future studies and will aid in unraveling the synchronicity of rapid climatic transitions in different

climate archives during the Last Glacial Period.

## Declaration of interests

The authors declare that they have no known competing financial interests or personal relationships that could have appeared to influence the work reported in this paper.

## CRedit authorship contribution statement

**Sunniva Rutledal:** Conceptualization, Investigation, Visualization, Writing - original draft. **Sarah M.P. Berben:** Conceptualization, Writing - review & editing, Supervision. **Trond M. Dokken:** Supervision, Funding acquisition. **Willem G.M. van der Bilt:** Investigation, Visualization, Writing - review & editing. **Jan Magne Cederstrøm:** Investigation, Visualization, Writing - review & editing. **Eystein Jansen:** Writing - review & editing, Supervision, Project administration, Funding acquisition.

## Acknowledgement

The research leading to these results has received funding from the European Research Council under the European Community's Seventh Framework Program (FP7/2007–2013)/ERC grant agreement 610055 as part of the ice2ice project. We thank Dr. Chris Hayward for his assistance with the use of the electron microprobe at the Tephra Analysis Unit, University of Edinburgh. We thank Dr. Eivind Støren from EARTHLAB, Department of Earth Science, University of Bergen for his guidance in using the CT scanner. We would also like to thank Nontje Marie Rücker for help in sample preparation and the R/V G.O. Sars and the ice2ice GS16-204 cruise crew members for retrieving the material used in this study. We also thank the IMAGES program and the R/V Marion Dufresne crew on leg MD114 for retrieving the MD99-2284 material. Siwan Davies and a second reviewer are thanked for their constructive feedback that greatly improved this manuscript.

## Appendix A. Supplementary data

Supplementary data to this article can be found online at <https://doi.org/10.1016/j.quascirev.2020.106247>.

## References

- Abbott, P.M., Bourne, A.J., Purcell, C.S., Davies, S.M., Scourse, J.D., Pearce, N.J.G., 2016. Last glacial period cryptotephra deposits in an eastern North Atlantic marine sequence: exploring linkages to the Greenland ice-cores. *Quat. Geochronol.* 31, 62–76.
- Abbott, P.M., Davies, S.M., Austin, W.E.N., Pearce, N.J.G., Hibbert, F.D., 2011. Identification of cryptotephra horizons in a North East Atlantic marine record spanning marine isotope stages 4 and 5a (~60,000–82,000 ka b2k). *Quat. Int.* 246, 177–189.
- Abbott, P.M., Griggs, A.J., Bourne, A.J., Chapman, M.R., Davies, S.M., 2018a. Tracing marine cryptotephra in the North Atlantic during the last glacial period: improving the North Atlantic marine tephrostratigraphic framework. *Quat. Sci. Rev.* 189, 169–186.
- Abbott, P.M., Griggs, A.J., Bourne, A.J., Davies, S.M., 2018b. Tracing marine cryptotephra in the North Atlantic during the last glacial period: protocols for identification, characterisation and evaluating depositional controls. *Mar. Geol.* 401, 81–97.
- Austin, W.E.N., Hibbert, F.D., Rasmussen, S.O., Peters, C., Abbott, P.M., Bryant, C.L., Blockley, S.P.E., Lane, C.S., Bronk Ramsey, C., Turney, C.S.M., 2012. The synchronization of palaeoclimatic events in the North Atlantic region during Greenland Stadial 3 (ca 27.5 to 23.3 kyr b2k). *Quat. Sci. Rev.* 36, 154–163.
- Austin, W.E.N., Wilson, L.J., Hunt, J.B., Hedges, R., Rhodes, E.J., 2004. The age and chronostratigraphical significance of North Atlantic Ash zone II. *J. Quat. Sci.* 19, 137–146.
- Beget, J., Mason, O., Anderson, P., 1992. Age, extent and climatic significance of the c. 3400 BP Aniakchak tephra, western Alaska, USA. *Holocene* 2, 51–56.
- Blockley, S.P.E., Bourne, A.J., Brauer, A., Davies, S.M., Hardiman, M., Harding, P.R., Lane, C.S., Macleod, A., Matthews, I.P., Pyne-O'donnell, S.D.F., Rasmussen, S.O.,

- Wulf, S., Zanchetta, G., 2014. Tephrochronology and the extended intimate (integration of ice-core, marine and terrestrial records) event stratigraphy 8–128 ka b2k. *Quat. Sci. Rev.* 106, 88–100.
- Blockley, S.P.E., Pyne-O'donnell, S.D.F., Lowe, J.J., Matthews, I.P., Stone, A., Pollard, A.M., Turney, C.S.M., Molyneux, E.G., 2005. A new and less destructive laboratory procedure for the physical separation of distal glass tephra shards from sediments. *Quat. Sci. Rev.* 24, 1952–1960.
- Bond, G.C., Lotti, R., 1995. Iceberg discharges into the North Atlantic on millennial time scales during the last glaciation. *Science* 267, 1005–1010.
- Borchardt, G.A., Aruscavage, P.J., Millard JR., H.T., 1972. Correlation of the Bishop Ash, a Pleistocene marker bed, using instrumental neutron activation analysis. *J. Sediment. Petrol.* 42, 301–306.
- Bourne, A.J., Cook, E., Abbott, P.M., Seierstad, I.K., Steffensen, J.P., Svensson, A., Fischer, H., Schuppach, S., Davies, S.M., 2015. A tephra lattice for Greenland and a reconstruction of volcanic events spanning 25–45 ka b2k. *Quat. Sci. Rev.* 118, 122–141.
- Bramlette, M.N., Bradley, W.H., 1941. Geology and biology of North Atlantic deep-sea cores between Newfoundland and Ireland: 1. Lithology and geologic interpretation. *U. S. Geol. Surv. Prof. Pap.* 196-A, 1–34.
- Brendryen, J., Hafliðason, H., Sejrup, H.P., 2010. Norwegian Sea tephrostratigraphy of marine isotope stages 4 and 5: prospects and problems for tephrochronology in the North Atlantic region. *Quat. Sci. Rev.* 29, 847–864.
- Brendryen, J., Hafliðason, H., Sejrup, H.P., 2011. Non-synchronous deposition of North Atlantic Ash Zone II in Greenland ice cores, and North Atlantic and Norwegian Sea sediments: an example of complex glacial-stage tephra transport. *J. Quat. Sci.* 26, 739–745.
- Davies, S.M., 2015. Cryptotephra: the revolution in correlation and precision dating. *J. Quat. Sci.* 30, 114–130.
- Davies, S.M., Wastegård, S., Rasmussen, T.L., Svensson, A., Johnsen, S.J., Steffensen, J.P., Andersen, K.K., 2008. Identification of the Fugloyarbanki tephra in the NGRIP ice core: a key tie-point for marine and ice-core sequences during the last glacial period. *J. Quat. Sci.* 23, 409–414.
- Davis, J.O., 1985. Correlation of late Quaternary tephra layers in a long pluvial sequence near Summer Lake, Oregon. *Quat. Res.* 23, 38–53.
- Dokken, T.M., Cruise-Members, 2016. Ice2Ice cruise GS16–204. In: Trond, M.D. (Ed.), *Bjerknes Climate Data Centre*.
- Dokken, T.M., Nisancioglu, K.H., Li, C., Battisti, D.S., Kissel, C., 2013. Dansgaard-Oeschger cycles: interactions between ocean and sea ice intrinsic to the Nordic seas. *Paleoceanography* 28, 491–502.
- Elliot, M., Labeyrie, L., Bond, G., Cortijo, E., Turon, J.-L., Tisnerat, N., Duplessy, J.-C., 1998. Millennial-scale iceberg discharges in the Irminger basin during the last Glacial Period: relationship with the Heinrich events and environmental settings. *Paleoceanography* 13, 433–446.
- Gehrels, M.J., Lowe, D.J., Hazell, Z.J., Newnham, R.M., 2006. A continuous 5300-yr Holocene cryptotephrostratigraphic record from northern New Zealand and implications for tephrochronology and volcanic hazard assessment. *Holocene* 16, 173–187.
- Griem, L., Voelker, A.H.L., Berben, S.M.P., Dokken, T.M., Jansen, E., 2019. Insolation and glacial meltwater influence on sea-ice and circulation variability in the northeastern Labrador Sea during the last Glacial Period. *Paleoceanography and Paleoclimatology* 34, 1689–1709. <https://doi.org/10.1029/2019PA003605>.
- Griggs, A.J., Davies, S.M., Abbott, P.M., Coleman, M., Palmer, A.P., Rasmussen, T.L., Johnston, R., 2015. Visualizing tephra deposits and sedimentary processes in the marine environment: the potential of X-ray microtomography. *G-cubed* 16, 4329–4343.
- Griggs, A.J., Davies, S.M., Abbott, P.M., Rasmussen, T.L., Palmer, A.P., 2014. Optimising the use of marine tephrochronology in the North Atlantic: a detailed investigation of the Faroe marine ash zones II, III and IV. *Quat. Sci. Rev.* 106, 122–139.
- Grönvold, K., Óskarsson, N., Johnsen, S.J., Clausen, H.B., Hammer, C.U., Bond, G., Bard, E., 1995. Ash layers from Iceland in the Greenland GRIP ice core correlated with oceanic and land sediments. *Earth Planet Sci. Lett.* 135, 149–155.
- Hafliðason, H., Eiríksson, J., Kreveld, S.V., 2000. The tephrochronology of Iceland and the North Atlantic region during the middle and late quaternary: a review. *J. Quat. Sci.* 15, 3–22.
- Hayward, C., 2012. High spatial resolution electron probe microanalysis of tephra and melt inclusions without beam-induced chemical modification. *Holocene* 22, 119–125.
- Heinrich, H., 1988. Origin and consequences of cyclic ice rafting in the Northeast Atlantic Ocean during the past 130,000 years. *Quat. Res.* 29, 142–152.
- Hunt, J., Hill, P.G., 2001. Tephrological implications of beam size-sample-size effects in electron microprobe analysis of glass shards. *J. Quat. Sci.* 16, 105–117.
- Jakobsson, S.P., 1979. Petrology of Recent Basalts of the Eastern Volcanic Zone, Iceland. Reykjavík.
- Jakobsson, S.P., Jonsson, J., Shido, F., 1978. Petrology of the western Reykjanes peninsula, Iceland. *J. Petrol.* 19, 669–705.
- Kuijpers, A., Andersen, M.S., Kenyon, N.H., Kunzendorf, H., Van Weering, T.C.E., 1998. Quaternary sedimentation and Norwegian sea overflow pathways around bill bay bank, northeastern Atlantic. *Mar. Geol.* 152, 101–127.
- Kvamme, T., Mangerud, J., Furnes, H., Ruddiman, W.F., 1989. Geochemistry of pleistocene ash zones in cores from the North Atlantic. *Nor. Geol. Tidsskr.* 69, 251–272.
- Lacasse, C., Sigurdsson, H., Carey, S., Paterne, M., Guichard, F., 1996. North Atlantic deep-sea sedimentation of Late Quaternary tephra from the Iceland hotspot. *Mar. Geol.* 129, 207–235.
- Lacasse, C., Werner, R., Paterne, M., Sigurdsson, H., Carey, S., Pinte, G., Saunders, A.D., Larsen, H.C., Clift, P.D., Ali, J.R., Beget, J., Cambay, H., Demant, A., Fitton, J.G., Fram, M.S., Fukuma, K., Gieskes, J.M., Holmes, M.A., Hunt, J.M., Lacasse, C., Larsen, L.M., Lykke-Andersen, H., Meltzer, A., Morrison, M.L., Nemoto, N., Okay, N., Saito, S., Sinton, C.W., Spezzaferri, S., Stax, R., Vallier, T.L., Vandamme, D., Wei, W., Werner, R., Wise JR., S.W., 1998. Long-range transport of Icelandic tephra to the Irminger basin, site 919. *Proc. Ocean Drill. Progr. Sci. Results* 152, 51–65.
- Lackschewitz, K.S., Wallrabe-Adams, H.-J., 1997. Composition and origin of volcanic ash zones in Late Quaternary sediments from the Reykjanes Ridge: evidence for ash fallout and ice-rafting. *Mar. Geol.* 136, 209–224.
- Larsen, G., 1981. Tephrochronology by microprobe glass analysis. In: Self, S., Sparks, R.S.J. (Eds.), *Tephra Studies*. NATO Advanced Study Institutes Series (Series C — Mathematical and Physical Sciences). Springer, Dordrecht.
- Le Maitre, R.W., Bateman, P., 1989. A Classification of Igneous Rocks and Glossary of Terms: Recommendations of the International Union of Geological Sciences Subcommittee on the Systematics of Igneous Rocks. Blackwell, Oxford.
- Moles, J.D., Mcgarvie, D., Stevenson, J.A., Sherlock, S.C., Abbott, P.M., Jenner, F.E., Halton, A.M., 2019. Widespread tephra dispersal and ignimbrite emplacement from a subglacial volcano (Torfajökull, Iceland). *Geology* 47, 577–580.
- Óladóttir, B.A., Sigmarsson, O., Larsen, G., Devidal, J.-L., 2011. Provenance of basaltic tephra from Vatnajökull subglacial volcanoes, Iceland, as determined by major- and trace-element analyses. *Holocene* 21, 1037–1048.
- Pearce, N.J.G., Alloway, B.V., Westgate, J.A., 2008. Mid-Pleistocene silicic tephra beds in the Auckland region, New Zealand: their correlation and origins based on the trace element analyses of single glass shards. *Quat. Int.* 178, 16–43.
- Perkins, M., Nash, W., Brown, F., Fleck, R., Perkins, M., 1995. Fallout tuffs of trapper creek, Idaho—A record of miocene explosive volcanism in the snake river plain volcanic province. *Bull. Geol. Soc. Am.* 107, 1484–1506.
- Ram, M., Donarummo, J., Sheridan, M., 1996. Volcanic ash from Icelandic ~57,300 Yr BP eruption found in GISP2 (Greenland) Ice Core. *Geophys. Res. Lett.* 23, 3167–3169.
- Ram, M.L., Gayley, R.L., 1991. Long-range transport of volcanic ash to the Greenland ice sheet. *Nature* 349, 401–404.
- Rasmussen, T.L., Wastegård, S., Kuijpers, A., Van Weering, T.C.E., Heinemeier, J., Thomsen, E., 2003. Stratigraphy and distribution of tephra layers in marine sediment cores from the Faeroe Islands, North Atlantic. *Mar. Geol.* 199, 263–277.
- Ruddiman, W.F., Glover, L.K., 1972. Vertical mixing of ice-rafted volcanic ash in North Atlantic sediments. *Geol. Soc. Am. Bull.* 83, 2817–2835.
- Sadatzki, H., Dokken, T.M., Berben, S.M.P., Muschitiello, F., Stein, R., Fahl, K., Menviel, L., Timmermann, A., Jansen, E., 2019. Sea ice variability in the southern Norwegian Sea during glacial Dansgaard-Oeschger climate cycles. *Sci. Adv.* 5.
- Sigurdsson, H., 1982. Útbreiddsla íslenskra gjóskulaga á botni Atlantshafs. In: THORARINSDÓTTIR, H. (Ed.), *Eldur er I Nordri*. Reykjavík: Sögufélag.
- Stoner, J.S., Channell, J.E.T., Hillaire-Marcel, C., 1998. A 200 ka geomagnetic chronostratigraphy for the Labrador Sea: indirect correlation of the sediment record to SPECMAP. *Earth Planet Sci. Lett.* 159, 165–181.
- Svensson, A., Andersen, K.K., Bigler, M., Clausen, H.B., Dahl-Jensen, D., Davies, S.M., Johnsen, S.J., Muscheler, R., Parrenin, F., Rasmussen, S.O., Röthlisberger, R., Seierstad, I.K., Steffensen, J.P., Vinther, B.M., 2008. A 60 000 year Greenland stratigraphic ice core chronology. *Clim. Past* 47–57.
- Svensson, A., Andersen, K.K., Bigler, M., Clausen, H.B., Dahl-Jensen, D., Davies, S.M., Johnsen, S.J., Muscheler, R., Rasmussen, S.O., Röthlisberger, R., Peder Steffensen, J., Vinther, B.M., 2006. The Greenland Ice Core Chronology 2005, 15–42 ka. Part 2: comparison to other records. *Quat. Sci. Rev.* 25, 3258–3267.
- Turney, C., 1998. Extraction of rhyolitic component of Vedde microtephra from minerogenic lake sediments. *J. Paleolimnol.* 19, 199–206.
- Van der Bilt, W.G.M., Rea, B., Spagnolo, M., Roerdink, D.L., Jørgensen, S.L., Bakke, J., 2018. NOVEL sedimentological fingerprints link shifting depositional processes to Holocene climate transitions in East Greenland. *Global Planet. Change* 164, 52–64.
- Van Kreveld, S., Sarnthein, M., Erlenkeuser, H., Grootes, P., Jung, S., Nadeau, M.J., Pflaumann, U., Voelker, A., 2000. Potential links between surging ice sheets, circulation changes, and the Dansgaard-Oeschger Cycles in the Irminger Sea, 60–18 Kyr. *Paleoceanography* 15, 425–442.
- Voelker, A.H.L., Hafliðason, H., 2015. Refining the Icelandic tephrochronology of the last glacial period — the deep-sea core PS2644 record from the southern Greenland Sea. *Global Planet. Change* 131, 35–62.
- Voelker, A.H.L., Sarnthein, M., Grootes, P.M., Erlenkeuser, H., Laj, C., Mazaud, A., Nadeau, M.-J., Schleicher, M., Mook, W.G., Van Der Plicht, J., 1998. Correlation of marine (super 14) C ages from the Nordic Seas with the GISP2 isotope record; implications for (super 14) C calibration beyond 25 ka BP. *Radiocarbon* 40, 517–534.
- Wastegård, S., Rasmussen, T.L., Kuijpers, A., Nielsen, T., Van Weering, T.C.E., 2006. Composition and origin of ash zones from marine isotope stages 3 and 2 in the North Atlantic. *Quat. Sci. Rev.* 25, 2409–2419.